Superconducting properties of mechanically exfoliated macro strain-free Fe(Se,Te) films

Len Masuda[1], Ryo Matsumoto[2], Yoshihiko Takano[2], Alberto Martinelli[3], Kai Walter[4], Alexandra Jung[4], Jens Hänisch[4], Kazumasa Iida[1,*]

[1] College of Industrial Technology, Nihon University, 1-2-1 Izumi-cho, Narashino, Chiba 275-8575, Japan
[2] National Institute for Materials Science (NIMS), Tsukuba, Ibaraki 305-0047, Japan
[3] CNR–SPIN Genova, Corso Perrone 24, 16152 Genova, Italy
[4] Institute for Technical Physics, Karlsruhe Institute of Technology, Hermann-von-Helmholtz-Platz 1, Eggenstein-Leopoldshafen, 76344, Germany

E-mail: iida.kazumasa@nihon-u.ac.jp

Abstract. The mismatch in lattice or thermal expansion coefficients between iron-based superconducting thin films and their substrates significantly impacts the superconducting transition temperature, T_c. Bulk single crystals, often used as strain-free references, are not ideal for comparison due to the non-equilibrium growth conditions of thin films. Free-standing thin films, grown under identical conditions and separated from the substrate, provide a more accurate basis for comparison. Here, we have successfully fabricated strain-free $FeSe_{0.5}Te_{0.5}$ thin films using two methods: i) peeling the superconducting layer with a razor blade, and ii) applying epoxy resin to a quartz substrate, placing a $FeSe_{0.5}Te_{0.5}$ thin film on top, securing it, and subsequently cleaving the film. The c-axis length of both films was nearly identical to that of bulk $FeSe_{0.5}Te_{0.5}$ single crystals. Additionally, a T_c of 13.6 K was observed for both relaxed films, closely matching the T_c of the corresponding bulk sample. Although the composition and T_c of the films are nearly identical to those of the single crystal, the upper critical field and irreversibility field are significantly different. This suggests that bulk single crystals, commonly used as strain-free references, may not be an ideal comparison with thin films.

1. Introduction

Since the discovery of LaFeAs(O,F) in 2008 [1], iron-based high-temperature superconductors, such as $Ae Fe_2As_2$ with the $ThCr_2Si_2$ structure (Ae=Sr, Ba) [2] and FeSe with the PbO structure [3] have been reported successively. From the early stages of research, these iron-based superconductors have been notable for their high upper critical field (H_{c2}) and low anisotropy. For instance, in epitaxial Fe(Se,Te) thin films with a superconducting transition temperature (T_c) of 20 K, H_{c2} exceeds 50 T at low temperatures, and the anisotropy is as small as 1 [4]. Furthermore, compared

to cuprates, the critical angle at which the grain boundary critical current density (J_c) begins to decay is nearly twice as large as for cuprates, and J_c starts to level off around 15° [5, 6]. These excellent properties make iron-based superconductors promising candidates for applications in high-field magnet wires. Currently, research is being actively conducted on (Ba,K)122 tape wires via powder-in-tube (PIT) method [7, 8, 9] and Fe(Se,Te) coated conductors, e.g., short length [10, 11, 12, 13, 14] and long length [15, 16].

In studies of physical properties, the pressure effect on iron-based superconductors has been a focus of attention since their discovery. For instance, in sintered $LaFeAsO_{0.89}F_{0.11}$, T_c is approximately 25 K; however, under applied pressure, T_c exhibits a dome-like variation, reaching 41 K at 4 GPa [17]. Similarly, applying isotropic pressure up to 7 GPa to sintered FeSe raises T_c from 8 K to 37 K, while at 14 GPa, T_c decreases to 6 K [18]. Moreover, induction of superconductivity by applying pressure to the parent compound $BaFe_2As_2$ has also been reported [19]. While these studies are primarily based on bulk materials, reports also exist on T_c variation [20, 21] and superconductivity induction [22, 23] in thin films due to epitaxial strain.

In general, for thin-film research, the reference for comparison is assumed to be bulk single crystals of the same composition. However, thin films grow under non-equilibrium conditions, making direct comparisons with bulk single crystals fabricated under near-equilibrium conditions inappropriate, if only strain is regarded. Therefore, the ideal reference for comparison is a free-standing thin film fabricated under identical growth conditions as the film on the substrate. One reported method for fabricating free-standing thin films involves using water-soluble $Sr_3Al_2O_6$ (SAO) as a sacrificial layer [24]. Examples include the direct growth of $GdBa_2Cu_3O_{7-\delta}$ on SAO [25], or the deposition of a perovskite oxide buffer-layer, such as $SrTiO_3$, followed by the growth of $YBa_2Cu_3O_{7-\delta}$ [26, 27] or FeSe [28]. In either case, immersing the film in deionized water or (Na or K)OH solution hydrolyzes the SAO layer, yielding a free-standing superconducting thin film. For Fe(Se,Te), a method utilizing a so-called structural avalanche to retrieve exfoliated films grown on CaF_2 substrates has been reported [29]. However, this method only yields films with small surface areas.

In this study, we fabricated mechanically exfoliated $FeSe_{0.5}Te_{0.5}$ thin films using two methods: (i) peeling the superconducting layer with a razor blade and (ii) applying epoxy resin to a quartz substrate, placing a $FeSe_{0.5}Te_{0.5}$ thin film on top, securing it, and then cleaving the film. Based on the *c*-axis lattice parameter and T_c, the mechanically exfoliated films are considered macro strain-free.

2. Experiments

2.1. Thin film growth

The $FeSe_{0.5}Te_{0.5}$ thin films were fabricated by pulsed laser deposition (PLD) using a KrF excimer laser (Compex 102F, Coherent). First, a 30–nm thick CeO_2 buffer layer

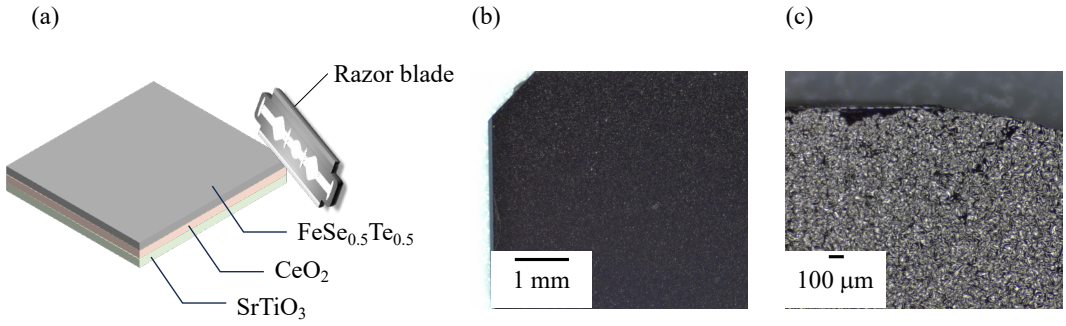


Figure 1. (a) Schematic illustration of the process used to peel the film with a razor blade. (b) Top view of the as-grown $FeSe_{0.5}Te_{0.5}$ film. (c) Top view of the peeled-off film.

was deposited on $SrTiO_3(001)$ substrates having a step-and-terrace surface (purchased from SHINKOSHA) and on Y-stabilized $ZrO_2(001)$ substrates (purchased from K&R creation). The growth temperature, oxygen pressure, energy density, and frequency were 600°C, 1 Pa, ϵ=1.5 J/cm^2, and f=1 Hz, respectively. The CeO_2 target was commercially sourced from Toshima. After deposition, the CeO_2-buffered $SrTiO_3$ was transferred to an ultra-high vacuum chamber (base pressure 1×10^{-7} Pa) without exposure to air for the subsequent growth of $FeSe_{0.5}Te_{0.5}$ having a thickness of 135–155 nm. The growth temperature, energy density, and frequency were 300°C, ϵ=1.5 J/cm^2, and f=5 Hz, respectively. We also fabricated Fe(Se,Te) films on $CaF_2(001)$ substrates (purchased from K&R creation) without CeO_2 buffer layer. The $FeSe_{0.5}Te_{0.5}$ target was prepared by quenching a melt [30].

2.2. Mechanically Exfoliation

A razor blade was used to separate the thin film from the substrate by gently touching the blade to the substrate's edge, as illustrated in fig. 1(a). This sample is hereafter referred to as Film A. Figures 1(b) and (c) show the top view of the as-grown film and the peeled-off film (Film A), respectively. As can be seen in fig. 1(c), flake-like thin fragments remained on the substrate. To create a free-standing membrane, Scotch tape was applied to Film A and subsequently transferred onto a quartz substrate. However, this attempt was unsuccessful. Only a small number of thin fragments were transferred, resulting in no electrical conduction. Hence, further measurements have been conducted on Film A exfoliated but still attached to the original substrate. It is worth noting that the fabrication of such films using a razor blade showed low reproducibility.

For Film B, epoxy resin (ThreeBond Fine Chemical) was applied to a quartz substrate, and an $FeSe_{0.5}Te_{0.5}$ thin film was placed on top. The assembly was then held at room temperature for 10 hours to allow the epoxy resin to fully cure [fig. 2(a)]. After curing, the substrate was peeled off, cleaving the superconducting layer and resulting in the formation of a strain-free thin film. Unlike Film A, the fabrication process for Film B proved to be highly reproducible. As shown in fig. 2(b), we have successfully produced

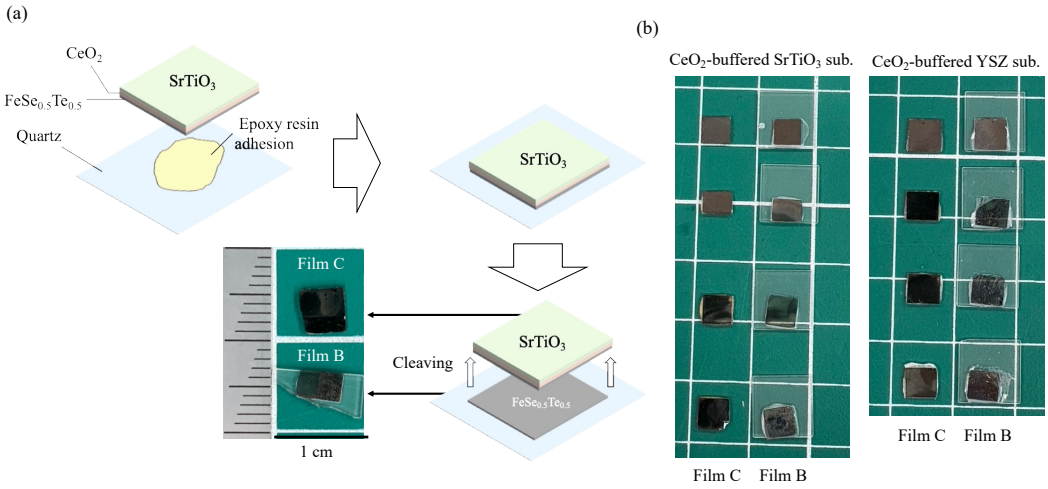


Figure 2. (a) Schematic illustration of the mechanically exfoliation process used to separate the $FeSe_{0.5}Te_{0.5}$ film from the substrate. The films obtained through this method are referred to as Film B and Film C, respectively. (b) Top view of several Film B samples, demonstrating that the method is highly reproducible. Each grid square is 1 cm×1 cm. YSZ stands for Y-stabilized ZrO_2.

more than 8 films by this method regardless of substrates (see also Supplementary Information, fig. S1). This method has ~~,in fact,~~ been widely used for photoemission spectroscopy measurements to obtain fresh cleavage planes in the vacuum chamber. The other side of the film is hereafter referred to as Film C.

Since epoxy resin can be removed by immersing the sample in acetone, it is possible to obtain a free-standing $FeSe_{0.5}Te_{0.5}$ membrane. This approach offers an alternative method for fabricating free-standing membranes, particularly for materials that are challenging to grow on sacrificial or buffered-sacrificial layers.

2.3. Characterization

Structural properties of the films were characterized using X-ray diffraction (XRD) with Cu Kα radiation (SmartLab, Rigaku) and scanning electron microscopy (SEM) equipped with energy dispersive X-ray spectrometry (EDX) (FEI-Apreo S LoVac).

The temperature dependence of the resistance was measured using a 4-probe method. The fabricated thin films were masked, and gold was deposited on contact pads using a sputtering apparatus (SC-701Mk II, Sanyu Electron). Double-sided tape was then attached to a d.c. rotator holder, and the thin film was secured on top. Cu wires were connected to the four electrode pads and fixed with silver paste. The applied magnetic field was oriented parallel to the crystallographic c-axis and ab-plane. The upper critical fields (H_{c2}) were defined as 90 % of the normal-state resistance R_n, which is defined as the deviation from the linear fit to the normal state. The irreversibility fields (H_{irr}) were defined as the noise level of R, typically around $10^{-5}R_n$.

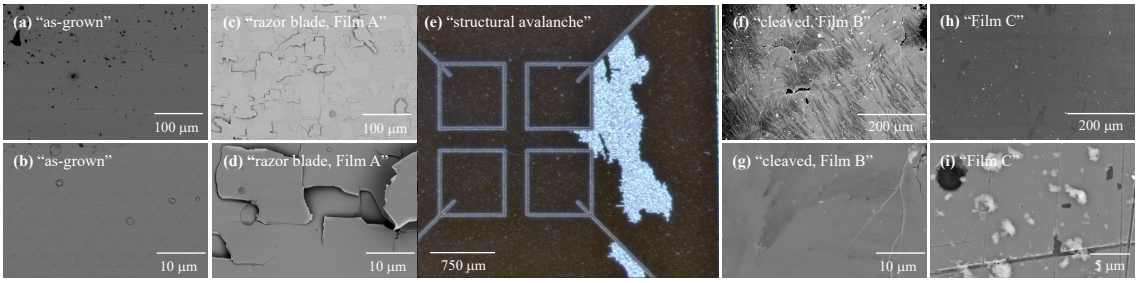


Figure 3. (a) Top-view SEM image of the as-grown $FeSe_{0.5}Te_{0.5}$ film and (b) its magnified view. (c) Exfoliated $FeSe_{0.5}Te_{0.5}$ film prepared with a razor blade (Film A) and (d) its close-up. (e) A snapshot of structural avalanches observed in Fe(Se,Te) after fabricating a micro-bridge by laser cutting. Please refer to the video for the progression of the structural avalanches (Supplementary information, video). (f) Film B and (g) its enlargement, showing dendritic features likely caused by strain relaxation. For comparison, (h) Film C and (i) its enlarged view exhibit a smoother surface without dendritic structures.

3. Results and discussions

Figure 3 presents SEM micrographs of the as-grown $FeSe_{0.5}Te_{0.5}$ film (a, b), the exfoliated Film A (c, d), cleaved Film B (f, g), and Film C (h, i). The SEM images [fig. 3(b)] reveal a lattice-like pattern on the surface of the as-grown film, with the lines oriented at 45° relative to the [100]/[010] directions of the substrate (i.e., parallel to the [110] of $FeSe_{0.5}Te_{0.5}$). No segregation was observed within this lattice pattern, which disappeared entirely after exfoliation when flake-like thin fragments cover the entire surface of the sample [figs. 3(c) and (d)]. This feature closely resembles the structural avalanche observed in Fe(Se,Te) thin films grown on CaF_2 [29]. Such structural avalanches are known to result from kinetic perturbations, such as those induced by the laser fabrication process [figs. 3(e) and Supplementary information, video]. Since the SEM image is not blurred across the entire observed area, indicating a constant focal distance, the surface of Film B is composed mainly of large, flat regions [figs. 3(f) and (g)]. Nevertheless, because the surface is not completely planar, local tilting of the crystal planes may occur, which could contribute to the peak broadening observed in the rocking curves (fig. 5). Furthermore, the dendritic structures observed are unlikely to be simple precipitates; rather, they likely formed as a consequence of the strain relaxation process. Notably, such dendritic features were not observed in Film C [figs. 3(h) and (i)].

EDX data averaged over 12 positions from Film B and C resulted in $Fe_{1.15\pm0.06}Se_{0.51\pm0.17}Te_{0.49\pm0.06}$, indicating that the nominal composition of Se and Te was transferred to the films. On the other hand, Fe was enriched during deposition.

Figures 4(a) and (b) confirm the biaxial texture of the as-grown $FeSe_{0.5}Te_{0.5}$ film. Compared to the as-grown thin film, the weaker diffraction intensity of the $00l$ (l=1, 2, 3 and 4) reflections in Film A is likely due to the detachment of $FeSe_{0.5}Te_{0.5}$ from the substrate, resulting in a reduced volume fraction contributing to the diffraction signal because of the larger orientation spread of the individual flakes. For Film A,

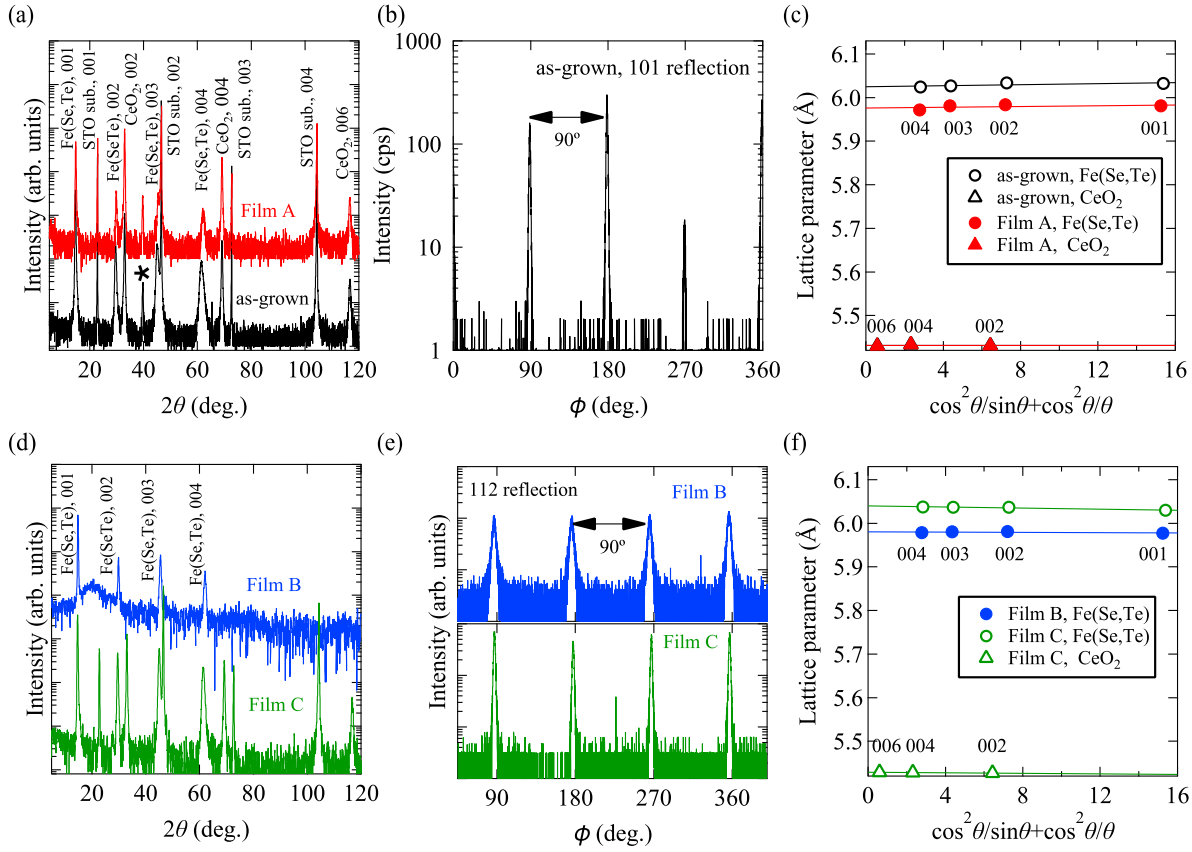


Figure 4. (a) X-ray diffraction pattern of $FeSe_{0.5}Te_{0.5}$ grown on a CeO_2-buffered $SrTiO_3$ substrate, showing the *c*-axis textured as-grown film and Film A. STO represents $SrTiO_3$. The asterisk is an impurity phase. (b) ϕ-scans of the 101 reflection for the as-grown film. (c) Nelson-Reily plots for the as-grown film and Film A, used to extract the out-of-plane lattice parameters of $FeSe_{0.5}Te_{0.5}$ and CeO_2. (d) 2θ–ω scans for Film B and C. (e) ϕ–scans of the 112 reflection for Film B and C. (e) Nelson-Reily plots for Film B and C.

the unchanged diffraction intensity of the $00l$ (l=2, 4, and 6) reflections of the CeO_2 buffer layer suggests that $FeSe_{0.5}Te_{0.5}$ detached at or above the interface between CeO_2 and $FeSe_{0.5}Te_{0.5}$. Another noteworthy observation is the shift of the $00l$ reflections of $FeSe_{0.5}Te_{0.5}$ in Film A to higher angles compared to the as-grown film. This shift is explained by the relaxation of compressive in-plane strain, which leads to a reduction in the *c*-axis length due to the Poisson effect. Similar results were observed in Film B [fig. 4(d)]. Since Film B was transferred to a quartz substrate, only the $00l$ reflections of $FeSe_{0.5}Te_{0.5}$ were observed. The 112 reflection of ϕ scans revealed that Film B remained in-plane-textured [fig. 4(e)] although it showed a larger full width at half maximum (FWHM) of the ϕ (average $\Delta\phi$=4.8°) than Film C (average $\Delta\phi$=2.0°). This is most likely due to a gradient in texture quality along the film thickness.

To extract the out-of-plane lattice parameters for $FeSe_{0.5}Te_{0.5}$ and the CeO_2 buffer-layer, Nelson–Riley extrapolation was employed [figs. 4(c) and (f)] [31]. The evaluated

Table 1. The c-axis length of $FeSe_{0.5}Te_{0.5}$ for as-grown, Film A, B, and C. The out-of-plane length of CeO_2 for as-grown, Film A, and Film C were also shown.

Samples	c-axis length of $FeSe_{0.5}Te_{0.5}$ (Å)	out-of-plane length of CeO_2 (Å)
as-grown	6.025±0.004	5.431±0.002
Film A	5.976±0.005	5.431±0.002
Film B	5.981±0.002	–
Film C	6.040±0.001	5.429±0.001
Bulk $FeSe_{0.5}Te_{0.5}$	∼5.98 [32]	
Bulk CeO_2		a=b=c=5.411 [36]

c-axis length for the as-grown film as well as Film A, B, and C are shown in table 1. The c-axis length of Film C is ~~almost identical~~ close to that of the as-grown film. Notably, the c-axis lengths of Film A and Film B are comparable to that of $FeSe_{1-x}Te_x$ single crystals with x∼0.5 (c∼5.98 Å)[32].

The out-of-plane lattice parameter of CeO_2 for as-grown film, Film A and C was ∼5.431 Å, which is slightly larger than the bulk value (5.411 Å). The coefficients of thermal expansion (CTE) for CeO_2 and $SrTiO_3$ between room temperature and CeO_2 deposition temperature are 11.5×10^{-6} /K [33] and 11×10^{-6} /K [34], respectively. Considering the error bars in lattice parameters, this means no CTE mismatch between CeO_2 and $SrTiO_3$. Assuming that CeO_2 grows coherently on a $SrTiO_3$ substrate, CeO_2 is expected to be subjected to in-plane tensile strain, resulting in an out-of-plane lattice constant smaller than 5.411 Å. In fact, the interface between CeO_2 and $SrTiO_3$ is sharp and free of any reaction layer [35]. However, the observed out-of-plane lattice constant of CeO_2 is ∼5.43 Å. Therefore, this increase cannot be explained by lattice or thermal expansion mismatch. On the other hand, it has been reported that oxygen deficiency in CeO_2 leads to lattice expansion [36]. In the present study, CeO_2 was deposited under a relatively low oxygen pressure of 1 Pa. Thus, it is considered that the CeO_2 films became oxygen-deficient, resulting in an increased lattice constant.

The variation in the lattice constants of $FeSe_{0.5}Te_{0.5}$ (i.e., as-grown → Film A and Film C → Film B) clearly indicates that the CeO_2-buffered $SrTiO_3$ (CeO_2/STO) influences the lattice structure of $FeSe_{0.5}Te_{0.5}$. A typical explanation would be the strain caused by lattice mismatch. Given that the lattice constant of CeO_2 is 3.825 Å($5.411/\sqrt{2}$) and the a-axis length of $FeSe_{0.5}Te_{0.5}$ is ∼3.8 Å, $FeSe_{0.5}Te_{0.5}$ should be under in-plane tensile strain, and its c-axis length is expected to be shortened. When the film is separated from the substrate, the c-axis would be expected to elongate. However, the c-axis length of the as-grown film and Film C is actually longer than that of the bulk material. This trend is similar to Fe(Se,Te) films grown on CaF_2 substrates with the same fluorite structure [37, 38, 39], and cannot be explained solely by lattice mismatch. Additionally, the c-axis lengths of Film A and B are shorter compared to the as-grown film and Film C. When Fe(Se,Te) is grown on CaF_2, the in-plane compressive strain leads to out-of-plane elongation as a consequence of the Poisson effect [40], which

refers to the strain response perpendicular to the direction of applied stress, assuming volume conservation. Two mechanisms have been proposed to explain the contraction of the *a*-axis: (i) substitution of F^- for Se^{2-} [37], and (ii) the difference in thermal expansion coefficients between CaF_2 and Fe(Se,Te) [38, 39]. Ref. [37] concluded that the primary cause of the lattice change is chemical substitution. To investigate this, we grew a $FeSe_{0.5}Te_{0.5}$ thin film on CaF_2 substrate and subsequently detached it, following the same procedure used for Film B. As a result, the *c*-axis length decreased from 6.006 Å to 5.928 Å (Supplementary information, fig. S1), indicating a relaxation of strain along the [001] direction by $\epsilon_{<001>,CaF_2} = (6.006 - 5.928)/6.006 \times 100 = 1.3\%$. Therefore, the influence of chemical substitution is considered to be relatively small.

Thus, the lattice constant of $FeSe_{0.5}Te_{0.5}$ films grown on CaF_2 is mainly governed by the difference in thermal expansion coefficients. In fact, the CTEs of CaF_2 and Fe(Se,Te) are $18\pm3\times10^{-6}$/K [41] and $\sim7.6\times10^{-6}$/K [42], respectively, showing a significant difference. Similarly, the strain relaxation rates along [001] between the as-grown film and Film A, and between Film C and Film B, are in the range of $\epsilon_{<001>CeO_2/STO}\sim$0.81-0.98%. The ratio of strain relaxation $\epsilon_{<001>,CaF_2}/\epsilon_{<001>,CeO_2/STO}$ is 1.3–1.6, which is approximately equal to the ratio of the CTEs of CaF_2 and CeO_2 (i.e., 1.2–1.8). Therefore, it can be concluded that the lattice constants of the as-grown film and Film C are primarily governed by the thermal expansion mismatch between CeO_2/STO and $FeSe_{0.5}Te_{0.5}$.

The rocking curves of the symmetric 00*l* (*l*=1, 2, 3 and 4) reflections of $FeSe_{0.5}Te_{0.5}$ were measured for as-grown film, Film A, B, and C [figs. 5(a)–(d)]. The average FWHM of the rocking curves for the four reflections was defined as $\Delta\omega$. In both methods for obtaining macro strain-free films, $\Delta\omega$ increased–slightly for Film A and somewhat more for Film B. One of the plausible reason is that the epoxy resin did not cure completely the $FeSe_{0.5}Te_{0.5}$ basal plane on the quartz substrate.

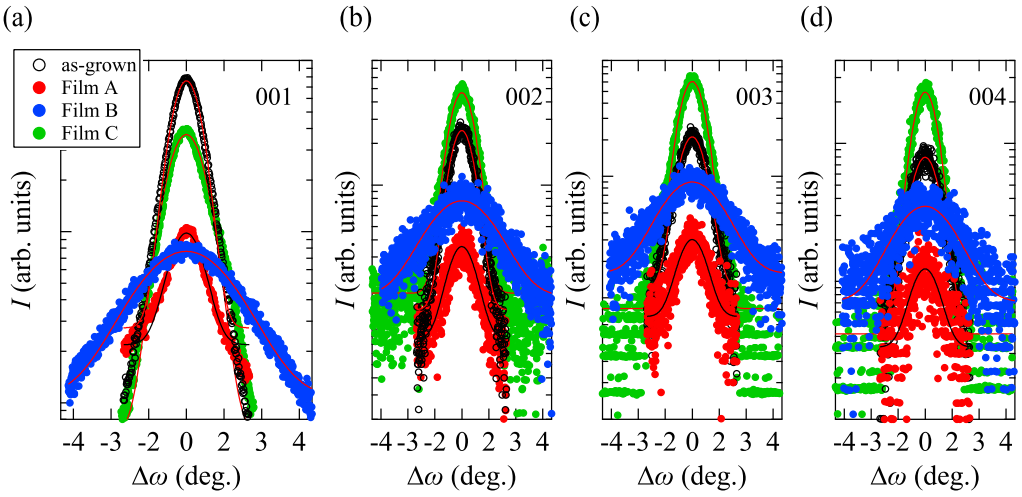


Figure 5. (a)–(d) Rocking curves of the 001, 002, 003, and 004 reflections for the as-grown film, Film A, B and C.

The electrical resistance of all films is similar, with a typical maximum at medium temperatures [fig. 6(a)]. Due to the unique structure of Film A, the normal-state resistance exhibited slight noise. In contrast, the normal-state resistance of Film B was stable and free of noise despite a broad transition. Shown in fig. 6(c) is the temperature dependence of magnetization for Film B. For comparison, the temperature dependence of the resistance is also presented. The zero-resistance temperature nearly coincides with the onset T_c of the diamagnetic signal, i.e., the temperature at which the zero-field cooling (ZFC) and field-cooling (FC) curves begin to diverge. However, the sample did not fully shield the magnetic field, likely due to the presence of macroscopic defects. Normal state resistance increased with decreasing temperature up to around 180 K, followed by decreasing until the superconducting transition for Film A. The same trend was observed for all films but the resistance maximum ($T_{R,max}$) appeared at 250 K, 220 K and 130 K for as-grown, Film C and Film B, respectively. There appears to be a weak correlation between $T_{R,max}$ and macrostrain, as the as-grown film and Film C (with a larger c-axis length) exhibited a higher $T_{R,max}$ than Film A and C (with smaller c-axis length). The temperature at which the resistivity reaches its maximum is identified as the onset temperature below which non-Fermi liquid behavior begins to develop in both resistivity and thermoelectricity [43]. This temperature thus marks a crossover from incoherent to coherent electronic transport, reflecting the emergence of strong electronic correlations in the system.

Both Film A and B displayed a lower T_c than the as-grown and Film C, which is attributed to the strain relaxation [fig. 6(b)]. The T_c for the as-grown film and Film C are 16.8–17.5 K, whereas the T_c for Film A and B were 13.6 K. Both relaxed Film A and B exhibited a broader transition width of approximately 5 K.

Although Film B is free of macroscopic strain at room temperature, it experiences tensile strain at low temperatures. Assuming that the temperature–dependent lattice contraction of $FeSe_{0.5}Te_{0.5}$ is identical to that of FeSe, the CTE mismatch between the quartz substrate and $FeSe_{0.5}Te_{0.5}$ is approximately 0.2%, resulting in in-plane tensile strain in Film B at low temperatures [44]. However, the impact on T_c of such tensile strain seems to be almost negligible, since Film A and B showed the same T_c of 13.6 K.

Figures 7(a)–(d) compare the magnetic phase diagrams of the four investigated films. The H_{c2} anisotropy, defined as the ratio of H_{c2} for $H\|ab$ to $H\|c$, was around 1.1 for the as-grown film, whereas for Film A, B, and C, it increased to a slightly larger value of 1.4.

Although the H_{c2} values of the as-grown film and Film C slightly differ for $H\|c$ [fig. 7(f)], the overall H_{c2} behavior for $H\|ab$ and $H\|c$ can be broadly classified into two groups: as-grown and Film C (strain), and Film A and B (strain-free). In contrast, the H_{c2} values for $H\|c$ in single crystals differ significantly from those of Film A and B, despite the fact that the T_c values for the single crystals and the strain-free films (i.e., Film A and B) are similar, around 14 K. The difference in H_{c2} and T_c between as-grown and Film C, and exfoliated films (Film A and B) are caused by macro-strain. On the other hand, the difference in H_{c2} between single crystals and strain-free films is

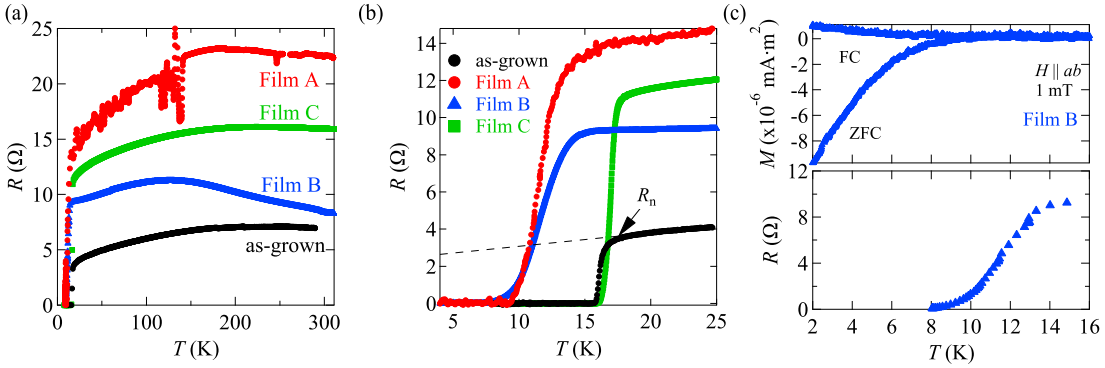


Figure 6. (a) Temperature dependence of resistance for the as-grown film, Film A, B, and C. (b) Enlarged view of (a) near the superconducting transition. The normal-state resistance R_n is defined as the deviation from the linear fit to the normal state region. The critical temperature T_c is defined as the intersection between the resistance trace and the line corresponding to $0.9R_n$. (c) Temperature dependence of magnetization (M–T) for Film B, together with the R–T curve, showing that the zero-resistance temperature nearly coincides with the onset temperature of the diamagnetic signal. ZFC and FC stand for zero-field cooling and field-cooling, respectively.

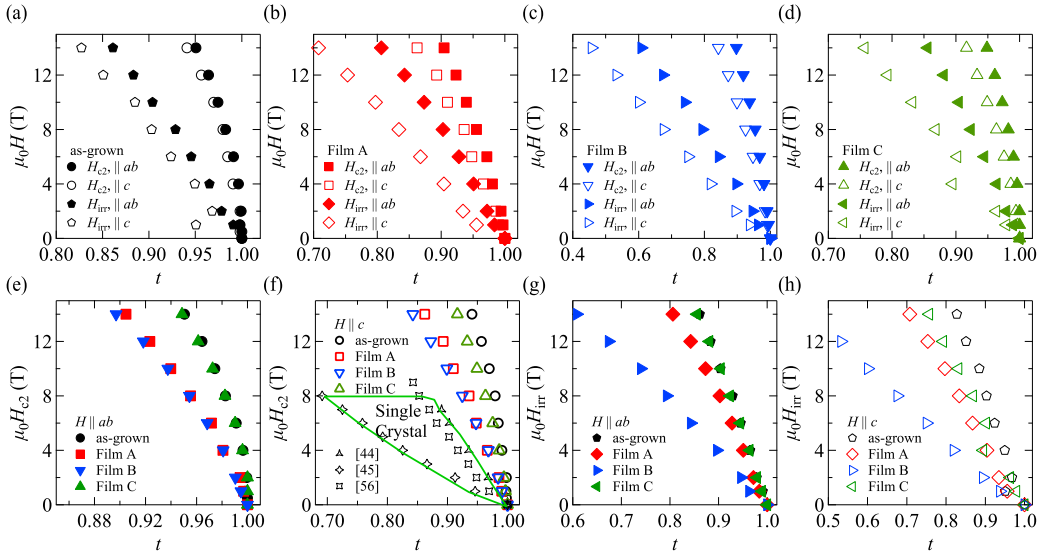


Figure 7. (a)–(d) Magnetic phase diagrams for the as-grown film, Film A, Film B, and Film C, respectively. The reduced temperature $t = T/T_c$ is used for the upper critical field H_{c2}, and $t = T/T_{irr}$ for irreversibility field H_{irr}, where T_c and T_{irr} are the critical temperature and irreversibility temperature, respectively. (e) H_{c2} as a function of reduced temperature $t = T/T_c$ for the as-grown film, Film A, B, and C with $H \| ab$. (f) H_{c2} as a function of reduced temperature with $H \| c$. For comparison, H_{c2} for single crystal are also shown [45, 46, 47]. (g) H_{irr} as a function of reduced temperature with $H \| ab$. (h) H_{irr} as a function of reduced temperature with $H \| c$.

likely due to growth-related defects. This also applies to single crystals, as H_{c2} varies, as shown in fig. 7(f). As the number of scattering centers due to defects increases, the

electron mean-free path l decreases. A reduced mean free path leads to a reduction in effective coherence length, and hence in an increase in H_{c2}. A similar mechanism may explain our results. These results suggest that bulk single crystals, which are typically considered strain-free references, may not provide an ideal basis for comparison with thin films.

The reduced-temperature dependence of H_{irr} for $H\|ab$ and $\|c$ in the as-grown film, Film A, B, and C is summarized in figs. 7(g)–(h). The H_{irr} values decrease in the order of the as-grown film, Film C, and strain-free films, following the same trend observed for H_{c2}. However, the decrease in H_{irr} for Film B is particularly pronounced, likely due to its large in-pane and out-of-plane FWHM, indicating poor crystallinity. It is also important to note that precise control of the $FeSe_{0.5}Te_{0.5}$ layer thickness is crucial; therefore, the superconducting properties of Film B remain significantly uncertain (see Supplementary Information, fig. S1.)

A key novelty of the present work lies in the adoption of a mechanical exfoliation route to obtain strain-free Fe(Se,Te) thin films, in contrast to earlier approaches based on structural avalanche or sacrificial-layer techniques. The buffer-release [28] or avalanche [29] methods rely on complex substrate engineering. Freestanding films prepared from sacrificial SAO layers are typically restricted in size due to the crack formation during lift-off process. Hence, electrical transport measurements usually require additional microfabrication by focused ion beam (FIB) to prepare electrodes on such small samples. By comparison, the exfoliation process employed here physically detaches the film without chemical modification, yielding larger-area, strain-relieved films with clean interfaces that can be directly contacted for transport and structural studies. This enables a more rigorous comparison with bulk single crystals and allows us to isolate the effect of epitaxial strain on T_c and other superconducting parameters with higher fidelity. Moreover, the mechanical exfoliation strategy broadens the scope of strain-free film preparation to a wider variety of substrate/film systems where sacrificial layers are difficult to integrate, offering a versatile and transferable method for disentangling intrinsic and extrinsic contributions in thin-film superconductivity.

4. Conclusion

We successfully fabricated macro strain-free $FeSe_{0.5}Te_{0.5}$ thin films using two different methods, structural avalanche and cleaving. Both strain-free films exhibited a T_c of 13.6 K, which is nearly identical to that of single crystals of the same stoichiometry. The c-axis lattice parameter of these films was also close to that of single crystals with $x{\sim}0.5$ in $FeSe_{1-x}Te_x$, matching the nominal composition of the PLD target. Although the composition and T_c of the films are nearly identical to those of the single crystal, the upper critical field and irreversibility field are significantly different. This suggests that bulk single crystals, commonly used as strain-free references, may not be ideal comparison with thin films regarding strain states alone.

Acknowledgments

This work was supported by Japan-Germany Research Cooperative Program between JSPS and DAAD, Grant number JPJSBP120203506. This work was also carried out under the Visiting Researcher's Program of the Institute for Solid State Physics, the University of Tokyo (No.202204-MCBXG-0048, No.202305-MCBXG-0085).

References

[1] Kamihara Y, Watanabe T, Hirano M and Hosono H 2008 Iron-based layered superconductor La[$O_{1-x}F_x$]FeAs (x=0.05–0.12) with T_c=26 K *J. Am. Chem. Soc.* **130** 3296
[2] Rotter M, Tegel M and Johrendt D 2008 Superconductivity at 38 K in the Iron Arsenide ($Ba_{1-x}K_x$)Fe_2As_2 *Phys. Rev. Lett.* **101** 107006
[3] Hsu F-C *et al* 2008 Superconductivity in the PbO-type structure α-FeSe *PNAS* **105** 14262
[4] Tarantini C *et al* 2011 Significant enhancement of upper critical fields by doping and strain in iron-based superconductors *Phys. Rev. B* **84** 184522
[5] Iida K, Hänisch J and Yamamoto A 2020 Grain boundary characteristics of Fe-based superconductors *Supercond. Sci. Technol.* **33** 043001
[6] Hänisch J and Iida K 2020 Grain Boundaries in Fe-Based Superconductors. In: Mele P *et al*. *Superconductivity* Springer, Cham.
[7] Pyon S *et al* 2021 Fabrication of small superconducting coils using (Ba,A)Fe_2As_2 (A: Na, K) round wires with large critical current densities *Supercond. Sci. Technol.* **34** 105008
[8] Dong C, Xu Q and Ma Y 2024 Towards high-field applications: high-performance, low-cost iron-based superconductors *National Science Review nwae122* https://doi.org/10.1093/nsr/nwae122
[9] Malagoli A *et al* 2024 Development of a Scalable Method for the Synthesis of High Quality (Ba,K)-122 Superconducting Powders *IEEE Trans. Appl. Supercond.* **35** 7300305
[10] Si W *et al* 2011 Iron-chalcogenide $FeSe_{0.5}Te_{0.5}$ coated superconducting tapes for high field applications *Appl. Phys. Lett.* **98** 262509
[11] Si W *et al* 2012 High current superconductivity in $FeSe_{0.5}Te_{0.5}$-coated conductors at 30 tesla *Nat. Commun.* **4** 1347
[12] Sylva G *et al* 2019 Fe(Se,Te) coated conductors deposited on simple rolling-assisted biaxially textured substrate templates *Supercond. Sci. Technol.* **32** 084006
[13] Thomas A A *et al* 2021 Comparative study of Fe(Se,Te) thin films on flexible coated conductor templates and single-crystal substrates *Supercond. Sci. Technol.* **34** 115013
[14] Piperno L *et al* 2024 Low-cost architecture for iron-based coated conductors *iScience* **27** 111032
[15] Liu L *et al* 2023 Fabrication of Meter-Long Class Fe(Se,Te)-Coated Conductors with High Superconducting Performance *Adv. Eng. Matter.* **25** 2201536
[16] Liu L, Li Y, Mou S, Miao C, Zhu R, Li R 2024 Development of Fe(Se,Te) Coated Conductors by PLD Process for High Magnetic Field Applications *IEEE Trans. Appl. Supercond.* **35** 6600704
[17] Takahashi H, Igawa K, Arii K, Kamihara Y, Hirano H and Hosono H 2008 Superconductivity at 43 K in an iron-based layered compound $LaO_{1-x}F_xFeAs$ *Nature* **453** 376
[18] Margadonna S *et al* 2009 Pressure evolution of the low-temperature crystal structure and bonding of the superconductor FeSe (T_c=37 K) *Phys. Rev. B* **80** 064506
[19] Kimber S *et al* 2009 Similarities between structural distortions under pressure and chemical doping in superconducting $BaFe_2As_2$ *Nat. Mater.* **8** 471
[20] Bellingeri E *et al* 2010 T_c=21 K in epitaxial $FeSe_{0.5}Se_{0.5}$ thin films with biaxial compressive strain *Appl. Phys. Lett.* **96** 102512
[21] Iida K *et al* 2009 Strong T_c dependence for strained epitaxial $Ba(Fe_{1-x}Co_x)_2As_2$ thin films *Appl. Phys. Lett.* **95** 192501

[22] Engelmann J *et al* 2013 Strain induced superconductivity in the parent compound $BaFe_2As_2$ *Nat. Commun.* **4** 2877
[23] Kang J *et al* 2020 Superconductivity in undoped in $BaFe_2As_2$ by tetrahedral geometry design *PNAS* **117** 21170
[24] Lu D *et al* 2016 Synthesis of freestanding single-crystal perovskite films and heterostructures by etching of sacrificial water-soluble layers *Nat. Mater.* **15** 1255–1260
[25] Xie Z, Li Z, Lu H, Wang Y and Liu Y 2021 Etching $Sr_3Al_2O_6$ sacrificial layer to prepare freestanding GBCO films with high critical current density *Ceramic International* **47** 13528
[26] Chen Z *et al* 2019 Freestanding crystalline $YBa_2Cu_3O_{7-x}$ heterostructure membranes *Phys. Rev. Mater.* **3** 060801(R)
[27] Jia Z *et al* 2023 Self-passivated freestanding superconducting oxide film for flexible electronics *Appl. Phys. Rev.* **10** 031401
[28] Shiogai J and Tsukazaki A 2023 Superconducting FeSe membrane synthesized by etching of water-soluble $Sr_3Al_2O_6$ layer *Appl. Phys. Lett.* **122** 052602
[29] Zhang H-F *et al* 2021 Evolution of Superconducting Properties in $Fe_{1.1}Se_{0.8}Te_{0.2}$ Films Before and After Structure Avalanche *ACS Appl. Mater. Interfaces* **13** 42138
[30] Palenzona A *et al* 2012 A new approach for improving global critical current density in $Fe(Se_{0.5}Te_{0.5})$ polycrystalline materials *Supercond. Sci. Technol.* **25** 115018
[31] Nelson J B and Riley D P 1945 An experimental investigation of extrapolation methods in the derivation of accurate unit-cell dimensions of crystals *Proc. Phys. Soc.* **57** 160
[32] Mukasa M *et al* 2021 High-pressure phase diagrams of $FeSe_{1-x}Te_x$: correlation between suppressed nematicity and enhanced superconductivity *Nat. Commun.* **12** 381
[33] Mogensen M, Sammes N M, Tompsett G A 2000 Physical, chemical and electrochemical properties of pure and doped ceria *Solid State Ionics* **129** 63–94
[34] de Ligny D and Pascal R 1996 High-temperature heat capacity and thermal expansion of $SrTiO_3$ and $SrZrO_3$ perovskite *Phys. Rev B* **53** 3013
[35] Iida K *et al* 2024 Structural analysis and transport properties of [010]-tilt grain boundaries in Fe(Se,Te) *Sci. Technol. Adv. Mater.* **25** 2384829
[36] Brauer G and Gingerich K A 1960 HOCHTEMPERATUR-RÖNTGENUNTERSUCHUNGEN AN CEROXYDEN *J. Inorg. Nucl. Chem.* **16** 87–99
[37] Ichinose A *et al* 2013 Microscopic analysis of the chemical reaction between Fe(Se,Te) thin films and underlying CaF_2 *Supercond. Sci. Technol.* **26** 075002
[38] Imai Y, Nabeshima F and Maeda A 2017 Comparative Review on Thin Film Growth of Iron-Based Superconductors *Condens. Matter* **2** 25
[39] Yuan F *et al* 2017 The influence of the in-plane lattice constant on the superconducting transition temperature of $FeSe_{0.7}Te_{0.3}$ thin films *AIP Advances* **7** 0655015
[40] Hänisch J, Iida K, Hühne R and Tarantini C 2019 Fe-based superconducting thin films–preparation and tuning of superconducting properties *Supercond. Sci. Technol.* **32** 093001
[41] Rakhimov N F, Nizamutdinov A S, Semashko V V, Popov P A, Marisov M A 2014 Measurements of thermal properties of crystals CaF_2: Ce^{3+} activated Yb^{3+} and Lu^{3+} ions *Journal of Physics: Conference Series* **560** 012018
[42] Xiao Y *et al* 2011 Physical properties, crystal and magnetic structure of layered $Fe_{1.11}Te_{1-x}Se_x$ superconductors *Eur. Phys. J. B* **82** 113–121
[43] Sato Y *et al* 2024 Non-Fermi liquid transport and strong mass enhancement near the nematic quantum critical point in $FeSe_xTe_{1-x}$ thin films arXiv:2412.18787v2
[44] Nakajima M, Ohata Y and Tajima S 2021 Control of band structure of FeSe single crystals via biaxial strain *Phys. Rev. Materials* **5** 044801
[45] Leo A *et al* 2014 Comparison of the pinning energy in $Fe(Se_{1-x}Te_x)$ compound between single crystals and thin films *Journal of Physics: Conference Series* **507** 012029
[46] Yakinci K 2022 Study on the Field Dependent Activation Energy, $U(H,T)$, Upper Critical Field, $H_{c2}(0)$, and Irreversibility Field, $\mu_0 H_{irr}$, Properties of Superconducting Single Crystal Ag Added

Fe(Se, Te) Alloys *J. Supercond. Nov. Magn.* **35** 2709

[47] Velasco-Soto D *et al* 2013 Upper critical fields in a $FeSe_{0.5}Te_{0.5}$ superconducting single crystal *J. Appl. Phys.* **113** 17E138